Science Advances
AAAS

Supplementary Materials for

Electronic skin as wireless human-machine interfaces for robotic VR

Yiming Liu, Chunki Yiu, Zhen Song, Ya Huang, Kuanming Yao, Tszhung Wong, Jingkun Zhou, Ling Zhao, Xingcan Huang, Sina Khazaee Nejad, Mengge Wu, Dengfeng Li, Jiahui He, Xu Guo, Junsheng Yu, Xue Feng, Zhaoqian Xie*, Xinge Yu*

*Corresponding author. Email: zxie@dlut.edu.cn (Z.X.); xingeyu@cityu.edu.hk (X.Y.)

Published 14 January 2022, *Sci. Adv.* **8**, eabl6700 (2022)
DOI: 10.1126/sciadv.abl6700

The PDF file includes:

Other Supplementary Material for this manuscript includes the following:

List of contents:

0.2 Hz. The experiment has been conducted for ~ 8 hrs, and only 7 bending sensors fall off from human skin in this process. The control panel and 5 actuators still attached on human skin after the test. (B) The adhesion time of each components during the 8-hr testing. "Photo Credit: Yiming Liu, Department of Biomedical Engineering, City University of Hong Kong".

Figure S10. The simulation of the buckling deformation across the entire circuits under uniaxial stretching. The FEA results of the equivalent strain distribution (**A**) and the out-of-plane displacement (**B**) in the copper layer for the entire circuits under 20% uniaxial stretching. The colors in (A) and (B) represent the equivalent strain and the out-of-plane displacement, respectively. The maximum strain remains well below the fracture limit (~5%) of copper.

Figure S11. The inductance changes of the energy harvesting antenna when stretched by 20% (**A**), and bent to a radius of ~2 cm (**B**).

Figure S12. The Q factor changes of the energy harvesting antenna when stretched by 20% (**A**), and bent to a radius of ~2 cm (**B**).

Figure S13. The S11 changes of the energy harvesting antenna when stretched by 20% (**A**), and bent to a radius of ~2 cm (**B**).

Figure S14. The electrical characteristics of the bending sensor. (**A, B**) optical images of the self-developed bending platform to bend the sensor automatically with programmable bending angles and frequencies. (**C, D**) Electrical response of the bending sensor with bending angle of 45° at a constant frequency of 1 Hz. (E) Electrical response of the bending sensor bent at different frequency with a constant bending angle of 45°. "Photo Credit: Yiming Liu, Department of Biomedical Engineering, City University of Hong Kong".

Figure S15. (**A**) Optical images of the volunteer's arm wearing the CL-HMI system under two skin conditions: dry at 0 h and sweating after 3 h. (**B**) Electrical responses of the 7 bending sensors with bending angle of ~ 75° under the two skin conditions. "Photo Credit: Yiming Liu, Department of Biomedical Engineering, City University of Hong Kong".

Figure S16. Electrical characteristics of the pressure sensor. (**A**) The frequency effect on the electrical performance of the pressure sensor as the stress frequency ranging from 0.5 Hz to 4 Hz. (**B, C**) Electrical response of the device during repeated cycles (> 8500) of pressing under 32.4 kPa at 1 Hz, where the signal amplitude after thousands cycles of pressing slightly change, proving the great stability and durability.

Figure S17. Optical images of the self-developed bending platform for automatically bending the flexible control panel repeatedly for 1 hour at a constant frequency of 1 Hz and angle of 75°. During the bending test, the control panel continuously output a constant voltage (3.3 V) without any signal interruption, indicating the stability of the control panel. "Photo Credit: Yiming Liu, Department of Biomedical Engineering, City University of Hong Kong".

Figure S18. The vibration amplitude of the actuator as a function of PWM current frequency at a constant peak voltage of 1.67 V. The actuator can yield the highest vibration amplitude of ~0.3 mm at the frequency of 250 Hz.

Figure S19. The largest transmission distance between the control panel and an Arduino board as mounting the control panel onto human forearm with four facing modes, including face to face (B1), face upsides (B2), face to back (B3), and back to back (B4). The transmission range of CL-HMI can cover ~3.42 m as it faces to the receiver.

Figure S20. The response time of a close-loop cycle which is affected by the distance between the control panel and the Arduino board receiver under Bluetooth mode. The ultrashort response time (< 4 μs) means users can wirelessly manipulate robot without detectable delay under Bluetooth mode.

Figure S21. The response time of a close-loop cycle as the control panel is mounted onto four human parts, including arm, abdomen, back, and leg, at a distance (sender and receiver) of 20 m. Under Wi-Fi mode, users can teleoperate robots with ultrashort response time (< 300 μs), less than human reaction time.

Figure S22. Response time of the whole process as teleoperating a robotic hand in Internet mode with five personal computers with different Central Processing Units (CPU).

Figure S23. The working time of the CL-HMI system as a function of its initial voltage under a full-load mode. The full-load working mode is capable of running a control panel with wirelessly communicating, 7 bending sensors, and 5 actuators.

Figure S24. Demonstrations of the control and feedback function of CL-HMI in remotely controlling a telecar. (**A**) A photo of the self-built runway for the telecar. (**B**) Optical images of a CL-HMI system mounted on the forearm and two bending sensors integrated on the knuckles. (**C, D**) Photos of fingers' gestures for teleoperating the telecar and the corresponding electrical signal outputs of the sensors. "Photo Credit: Yiming Liu, Department of Biomedical Engineering, City University of Hong Kong".

Figure S25. Demonstrations of the CL-HMI on human fingers in wirelessly controlling a telecar and the corresponding electrical signals of the bending sensors, including four situations teleoperating the vehicle backward to right, forward to right, and backward to left. " Photo Credit: Yiming Liu, Department of Biomedical Engineering, City University of Hong Kong".

Figure S26. Images of teleoperating a 7-DOF prosthetic hand to do various gestures and corresponding electrical signals of bending sensors mounted on different parts, including thumb (A1), index finger (A2), middle finger (A3), ring finger (A4), pinkie (A5), wrist (A6), and elbow (A7). "Photo Credit: Yiming Liu, Department of Biomedical Engineering, City University of Hong Kong".

Figure S27. Optical image of wires of bending sensors fixed by a tape on the back of the user's hand connecting to the CL-HMI system. "Photo Credit: Yiming Liu, Department of Biomedical Engineering, City University of Hong Kong".

Fig. S28. Demonstrations of accelerometers to control a 7-DOF robotic arm. (**A**) Optical image of the HMI system mounted onto human forearm with an accelerometer connected. (**B, C**). Optical images of the human wrist motions and corresponding electrical responses of the accelerometer for motion capturing. Here, the wrist motions contain bending down, up, left, right, and rotating. "Photo Credit: Yiming Liu, Department of Biomedical Engineering, City University of Hong Kong".

Figure S29. (**A**) The locations of the four control panels, bending sensors, and actuators of the CL-HMI on the human body to manipulate a13-DOF humanoid robot. (**B**) The optical images of the actuators mounted on target areas of human body, including forearm, upper arm, thigh, thigh side, tummy, and crus. (**C**) Electrical response of the bending sensors on 10 typical human body areas as they were bent to 30°, 45°, and 60°, respectively. "Photo Credit: Yiming Liu, Department of Biomedical Engineering, City University of Hong Kong".

Figure S30. The schematic diagram of the voltage divider circuit design. In this circuit, a fixed resistor (R_0) is connected to the bending sensor in series, and the microcontroller (MCU) is connected to read the voltage variance of the fixed resistor for calculating the voltage changes of the bending sensor.

Figure S31. Procedure of the microcontroller in the CL-HMI converting the voltage inputs from bending sensors into 2-byte values for later wireless data transmission by Bluetooth without information loss.

Figure S32. An experimenter wearing the CL-HMI system teleoperates the humanoid robot to walk. "Photo Credit: Yiming Liu, Department of Biomedical Engineering, City University of Hong Kong".

Figure S33. The PDMS thickness as a function of spinning speed of the spin coater with a constant spinning time of 10 s.

Movie S1. Optical video and finite element analysis of the actuator with the PET film central angle of 60° vibrating at the resonate frequency and power input of 250 Hz and 0.15 W, respective, as the CL-HMI provides the PWM current under a fixed duty cycle of 5: 5. The highest travelling distance of the actuator can reach to 0.3 mm.

Movie S2. A user wears the CL-HMI system to wirelessly control a telecare. The enlarged video showing his hand motions. Here, the CL-HMI consists of 2 bending sensors, fixed onto two index fingers for direction and speed controlling, and a control panel for data collection, analysis and wireless communication.

Movie S3. An experimenter wearing the CL-HMI system wireless controls the 7-DOF prosthetic arm with five actuating channels for haptic feedback. In this system, 7 bending sensors are mounted onto human hand joints for hand motion caption, and 5 actuators are attached to the five human fingertips for haptic feedback triggered by the five pressure sensors mounted onto the five prosthetic hand fingertips. Only one control panel is adopted for data collection, analysis, and wireless communication with the paired Arduino board for controlling the prosthetic hand.

Movie S4. An experimenter wearing the CL-HMI system teleoperates the 7-DOF prosthetic hand to grab a balloon with controlled force through the haptic feedback. Here, the CL-HMI system consists of 7 bending sensors, 5 actuators, and a control panel.

Movie S5. An experimenter wearing the CL-HMI system teleoperates the 7-DOF prosthetic hand to do oral sampling for detection of Sars-Cov-2 with controlled force through the haptic and visual feedback.

Movie S6. An experimenter wearing the CL-HMI system teleoperates a 7-DOF prosthetic hand to grasp a cup in Internet mode.

Movie S7. An experimenter wearing the CL-HMI system teleoperates a 13-DOF humanoid robot to take care of an artificial patient with haptic and visual feedback in real-time and Wi-Fi transmission mode. Here, the system consists of 13 bending sensor, 13 actuators, and 4 control panels, as shown in Supplementary Fig. 19.

Table S1. The reported flexible Human machine interface system in the last 10 years.

Communication mode	Sensors	Feedback system	Control panel	Controlling machine	Reference
Hard wire	EOG and EEG sensors	None	A hard box	Robotic arm	*28*
	Strain sensor		Hard substrate	Robotic hand	*29*
	Angular sensor		Personal computer	Robotic arm	*30*
	TENG sensor		Personal computer	Robotic hand	*18*
	Strain sensor		Arduino board	Robotic hand	*31*
	Pressure sensor		Personal computer	Robotic hand	*32*
	Strain sensor		Arduino board	Robotic hand	*33*
	TENG sensor		Arduino board	E-game	*34*
NFC	None	Vibratory actuator	Flexible circuit	E-game	*20*
Bluetooth	Acceleration sensor	None	Flexible circuit	Robotic arm	*35*
	EOG sensor		Hard substrate	wheel	*36*
	Pressure sensor		Personal computer	Mobile robot	*23*
	EMG sensor		Flexible circuit	Robotic arm	*11*
	Touch sensor		Hard substrate	E-game	*37*
	Strain sensor		Flexible circuit	Robotic arm	*22*
Wi-Fi	Inertial unit		Hard substrate	Robot	*38*
	EMG sensor		Personal computer	Quadrotor	*14*
Optical transmission	TENG sensor and modulator		Arduino board	Robotic hand	*2*

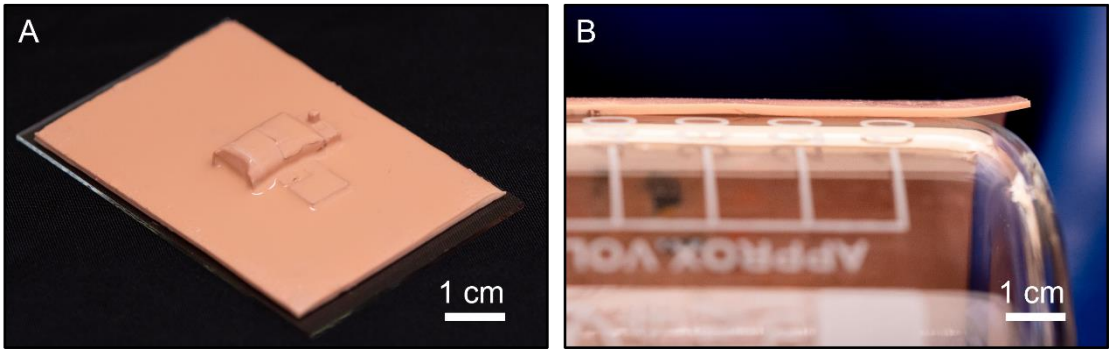

Figure S1

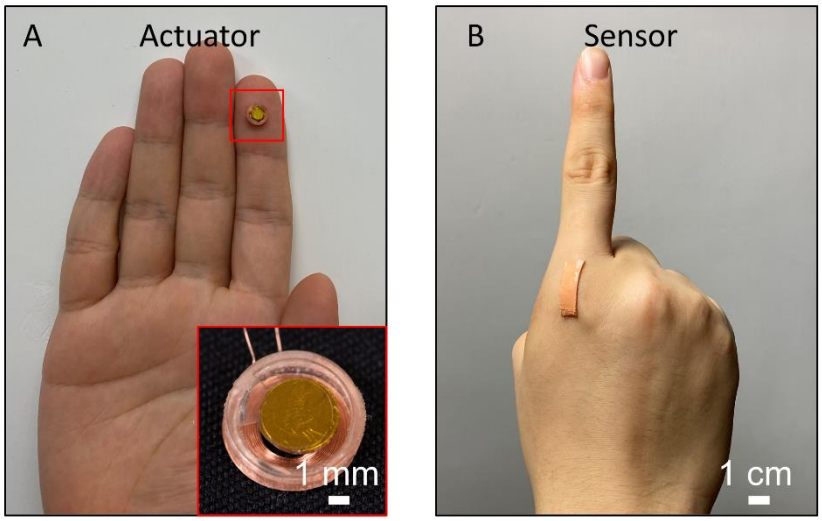

Figure S2

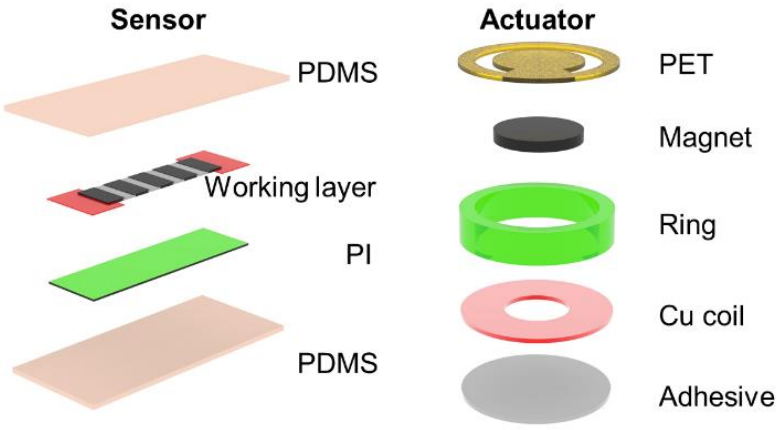

Figure S3

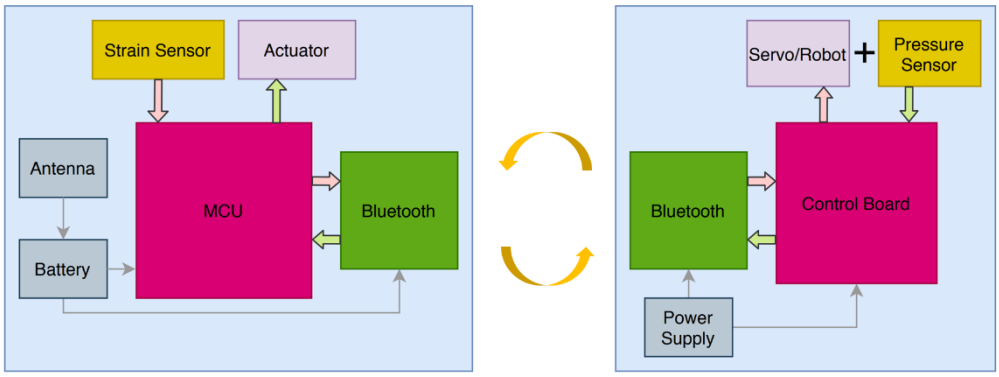

Figure S4

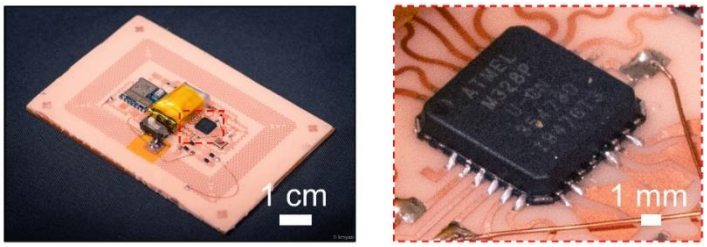

Figure S5

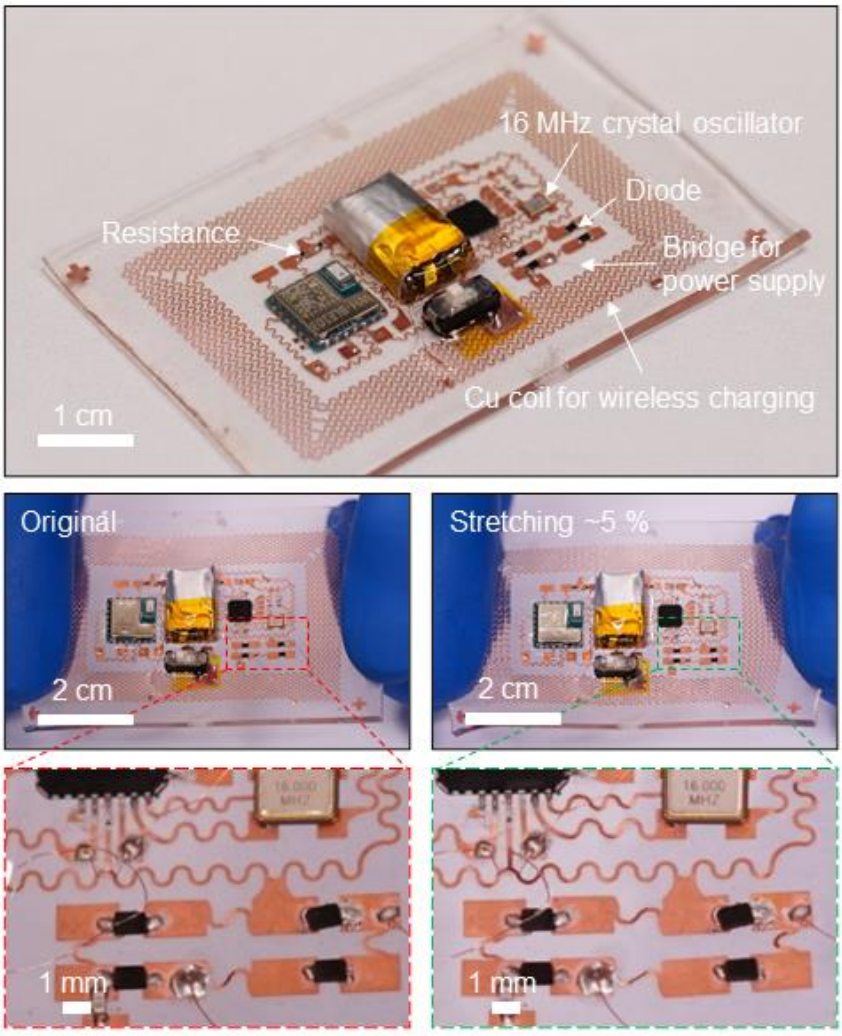

Figure S6

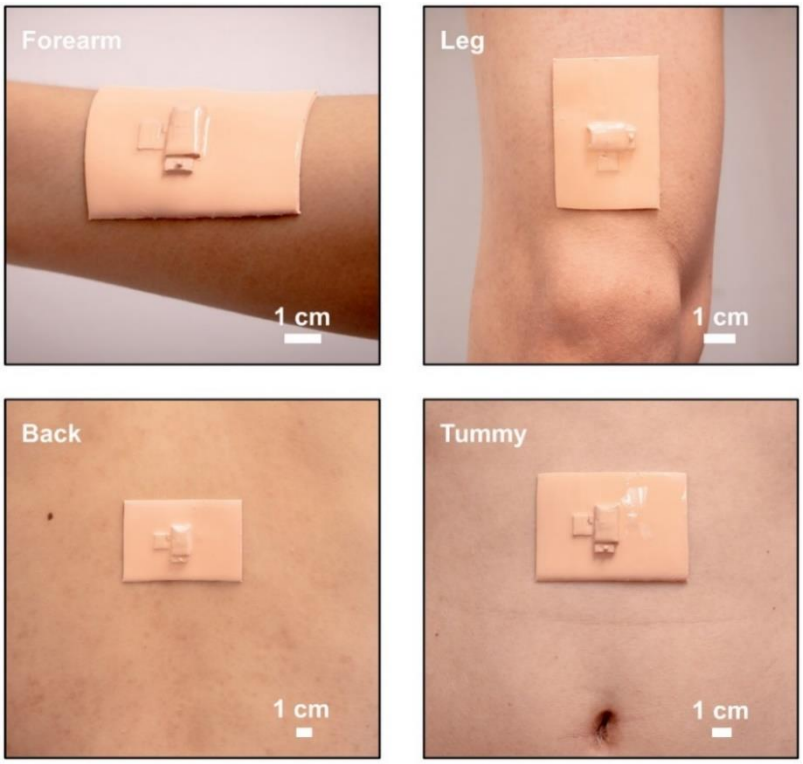

Figure S7

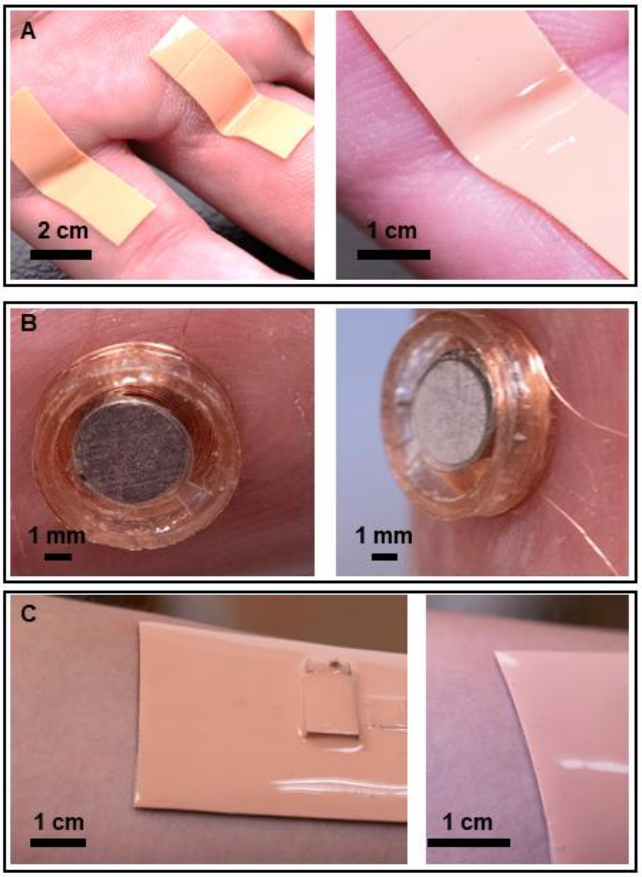

Figure S8

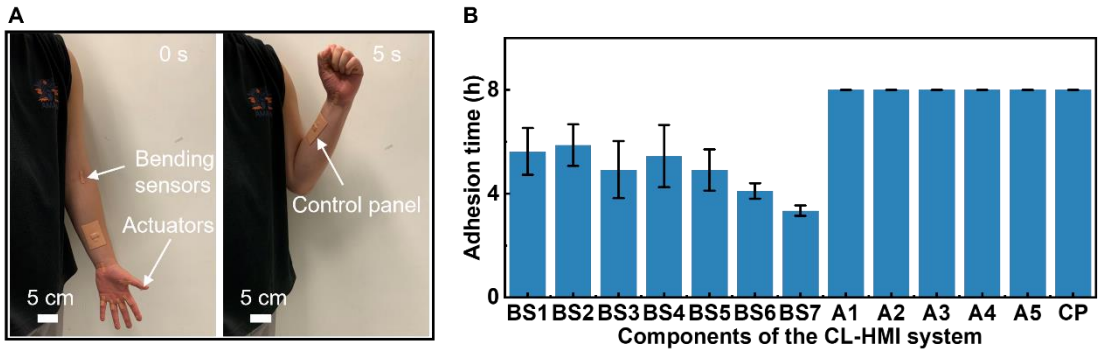

Figure S9

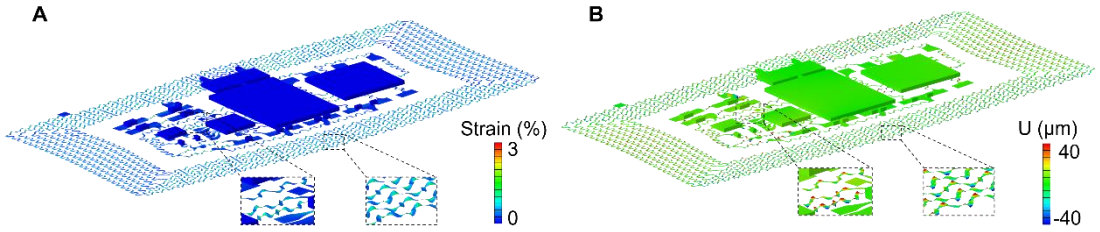

Figure S10

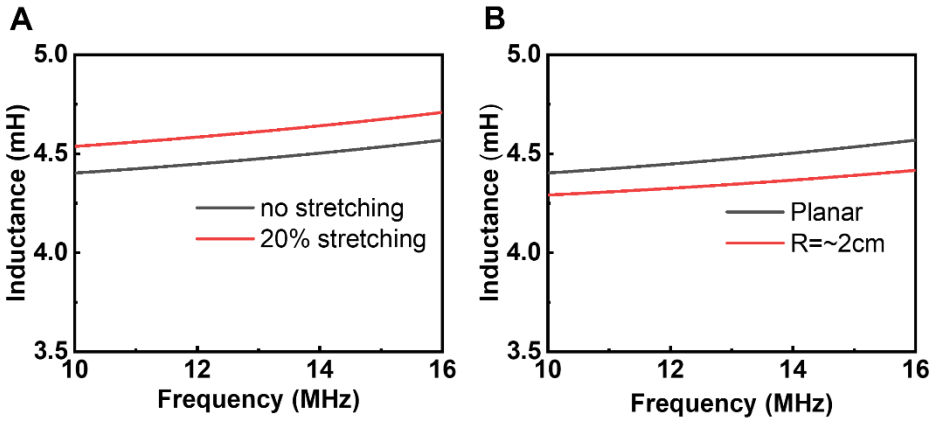

Figure S11

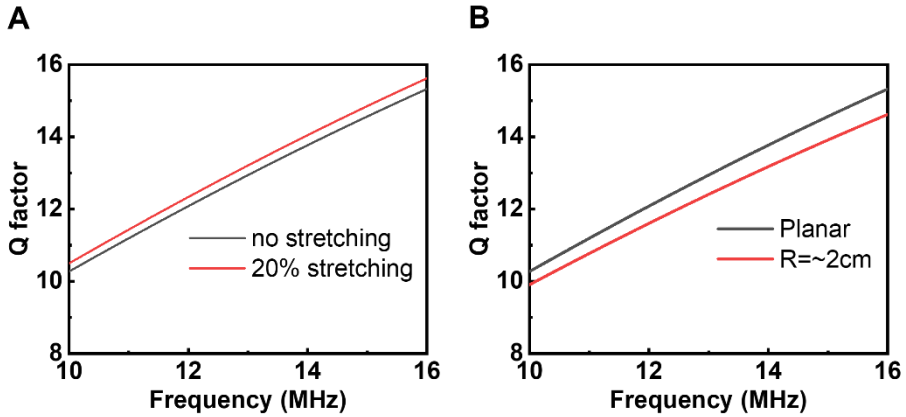

Figure S12

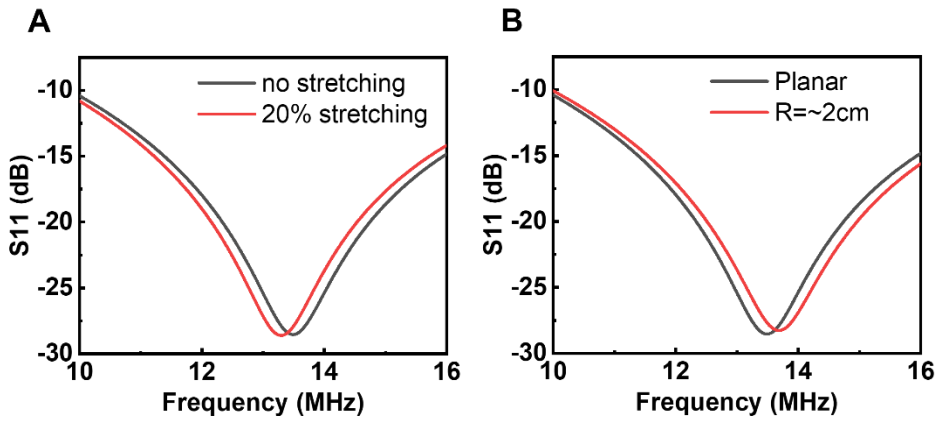

Figure S13

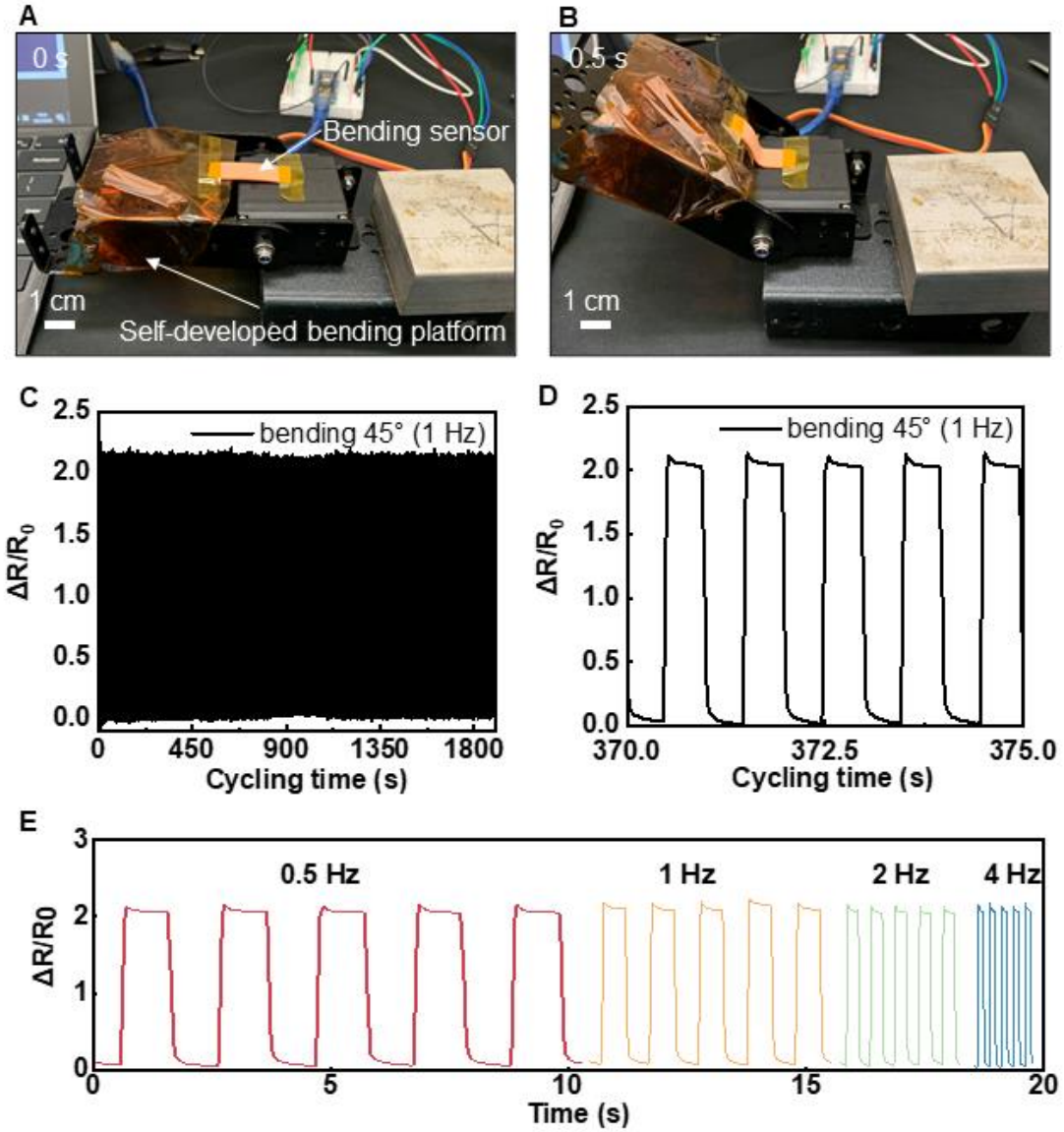

Figure S14

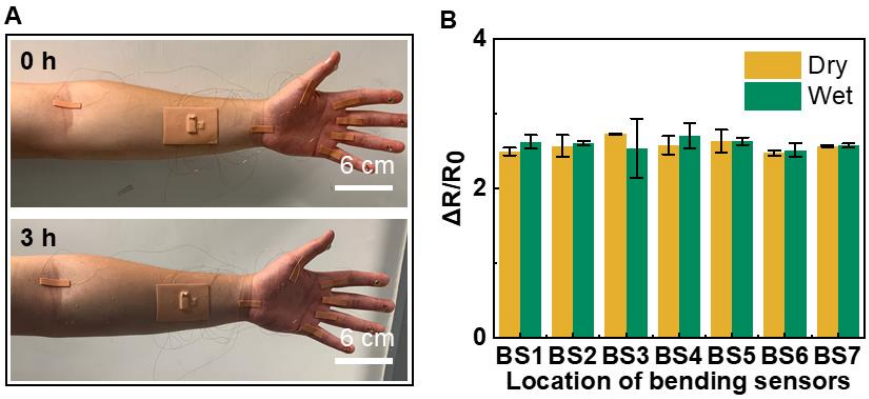

Figure S15

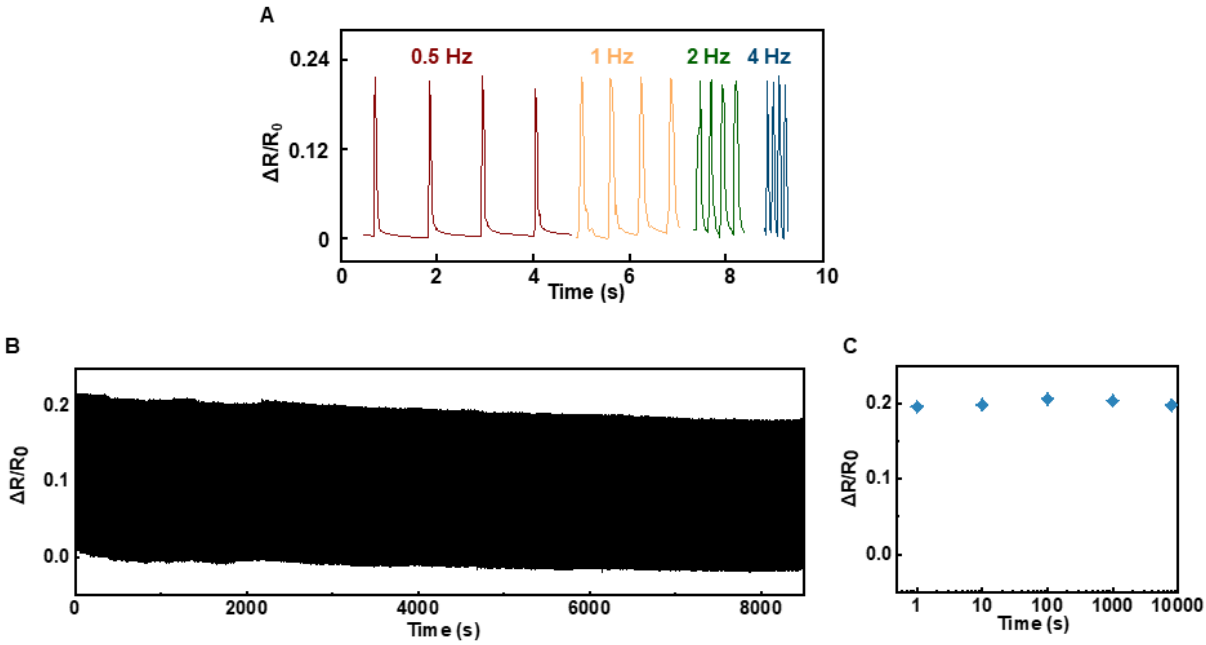

Figure S16

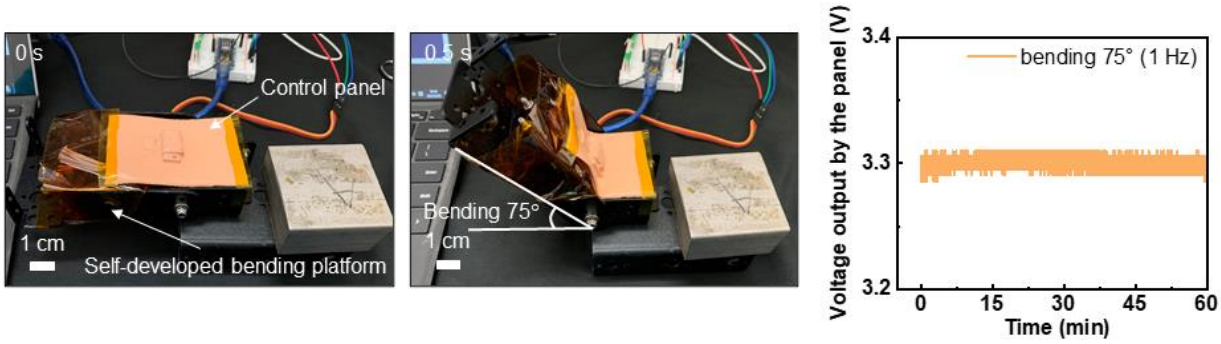

Figure S17

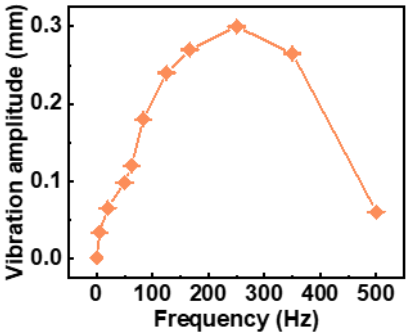

Figure S18

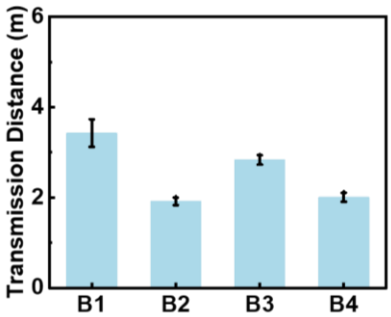

Figure S19

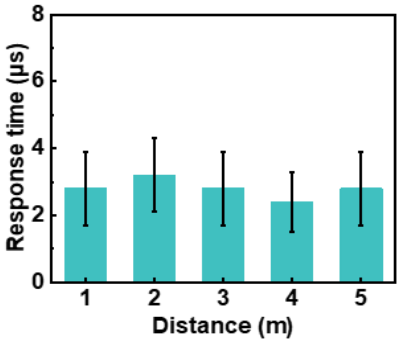

Figure S20

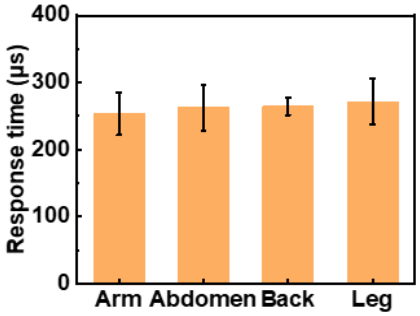

Figure S21

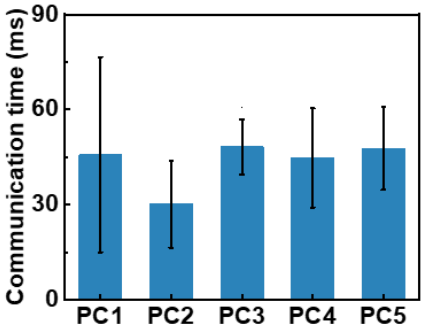

Senders	CPU model
Receiver	Inter® Core™ i7-4712HQ, 2.3 GHz
PC1	Inter® Core™ i5-7300U, 2.6 GHz
PC2	Inter® Core™ i7-6700HQ, 2.6 GHz
PC3	Inter® Core™ i7-9750H, 2.6 GHz
PC4	Inter® Core™ i7-10750H, 2.6 GHz
PC5	Inter® Core™ Pentium® 4415Y, 1.6 GHz

Figure S22

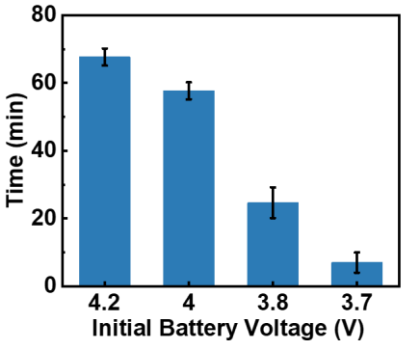

Figure S23

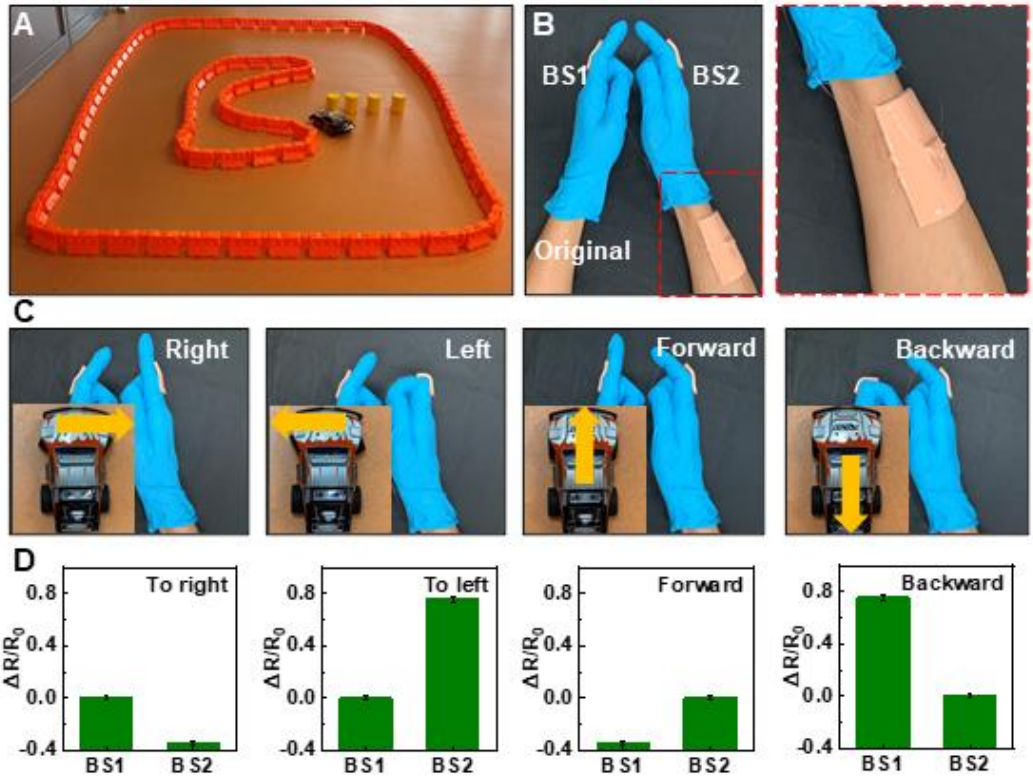

Figure S24

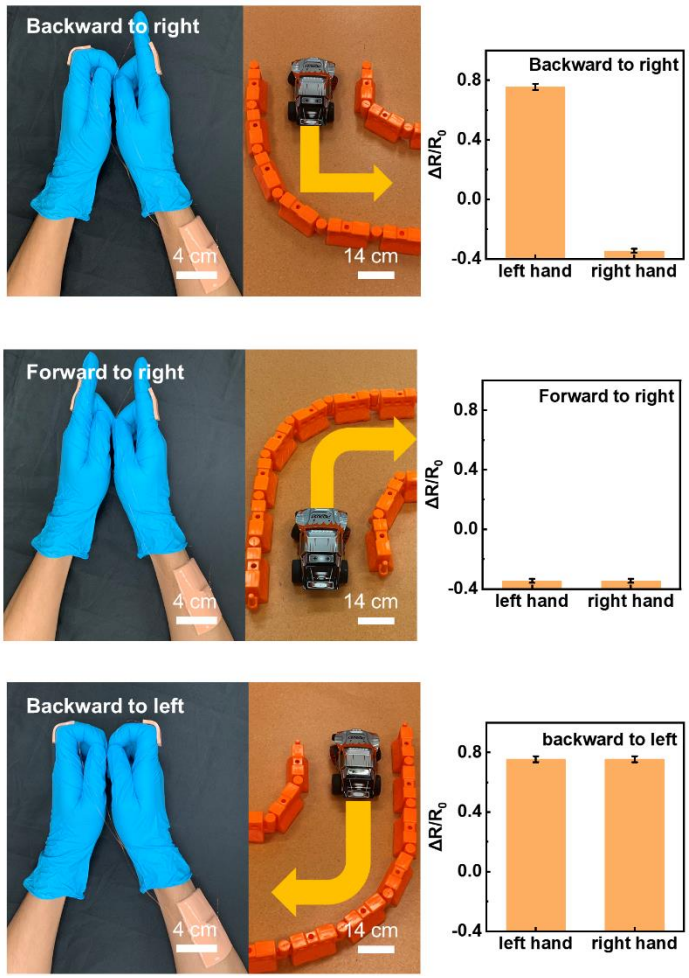

Figure S25

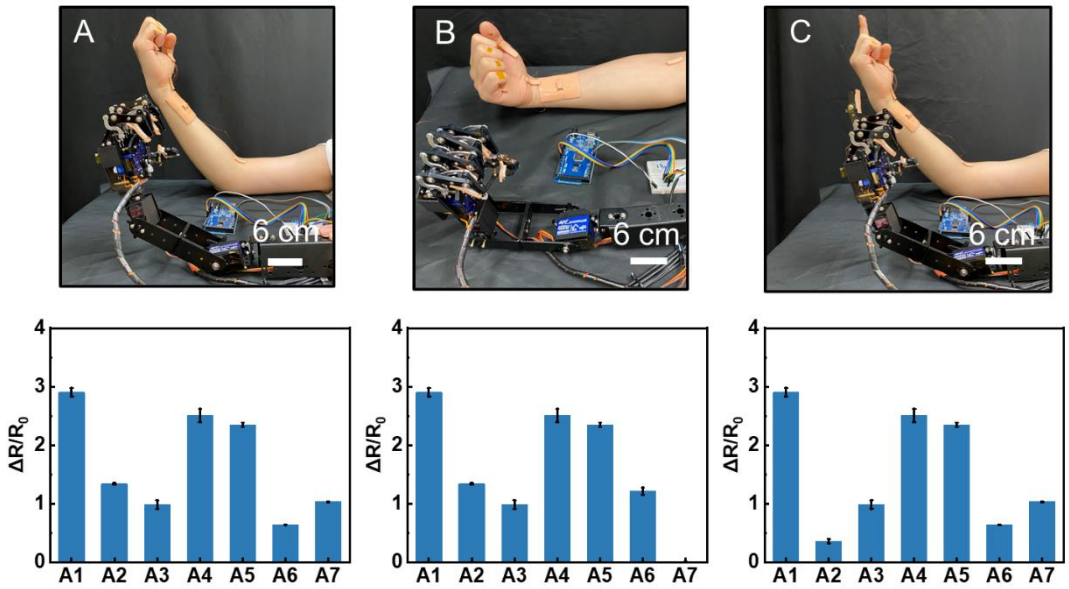

Figure S26

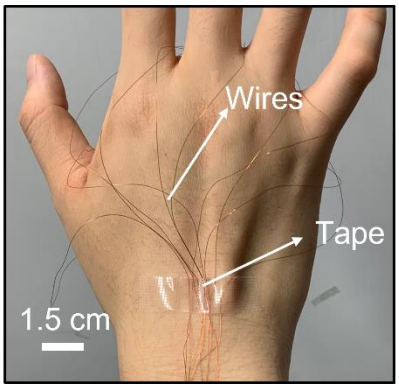

Figure S27

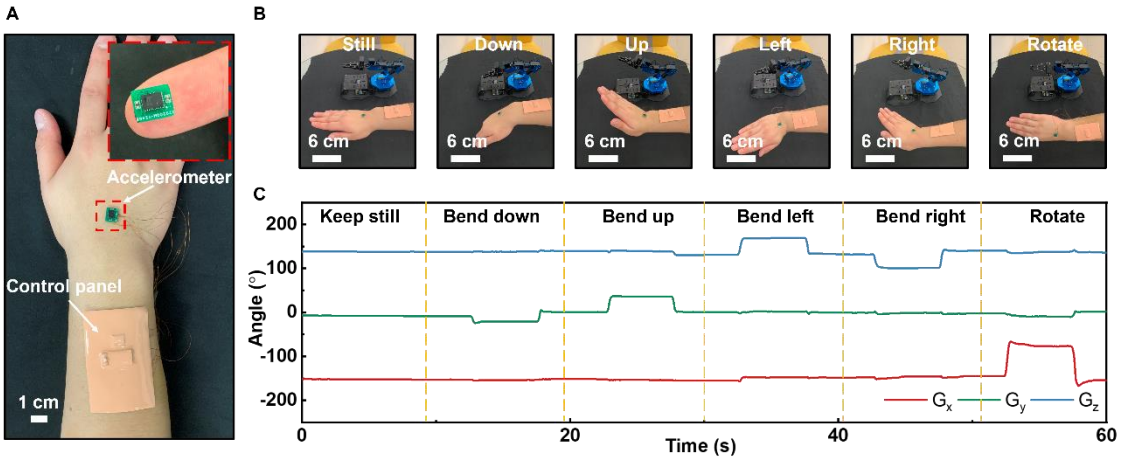

Figure S28

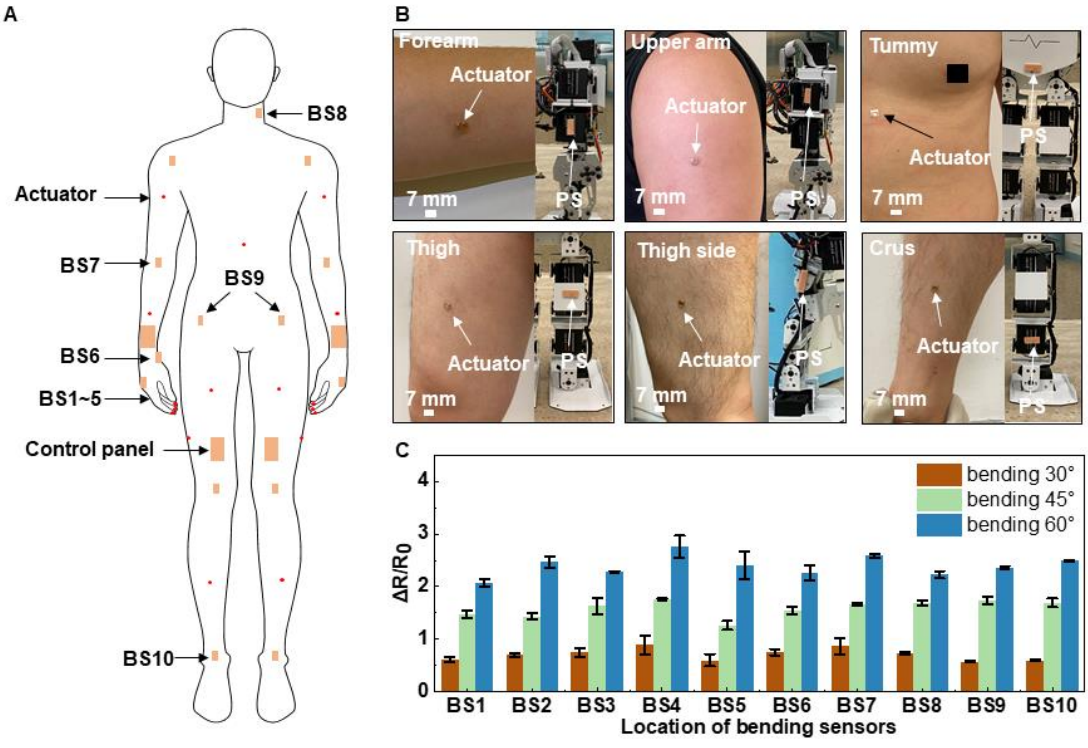

Figure S29

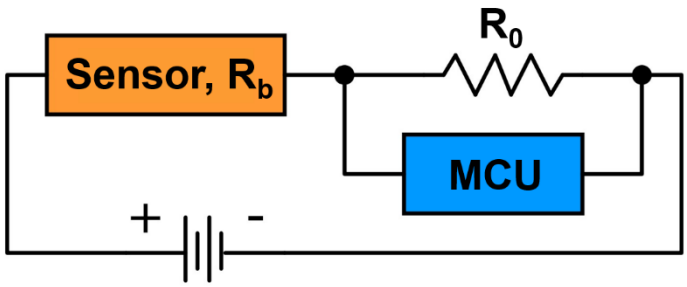

Figure S30

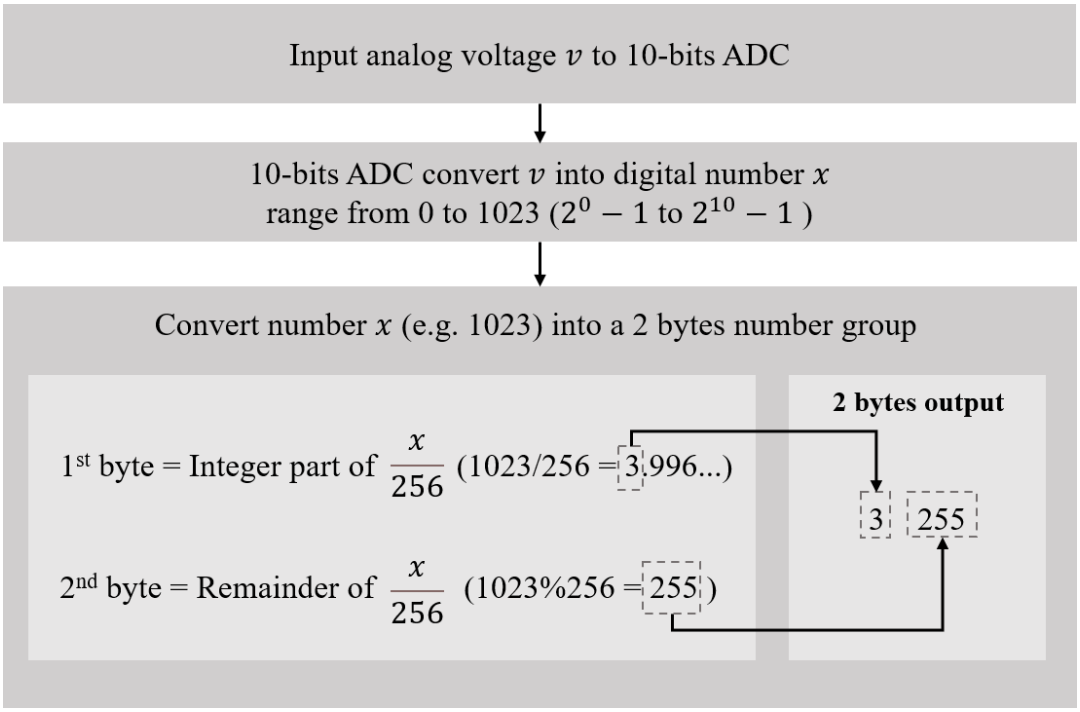

Figure S31

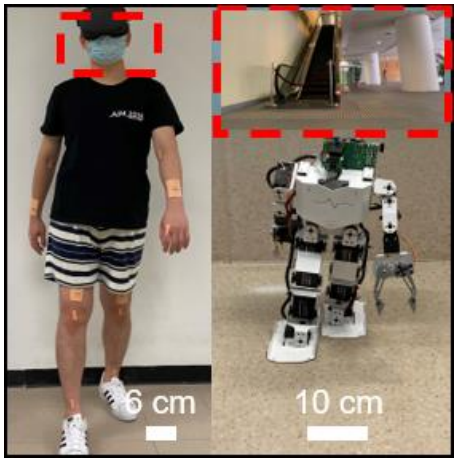

Figure S32

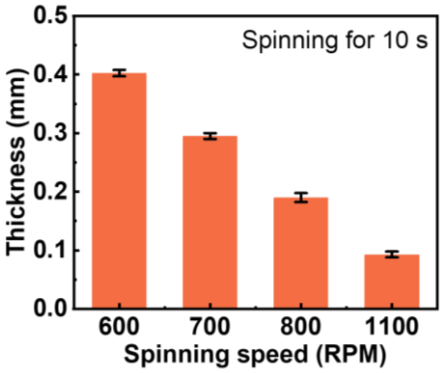
Spinning for 10 s
Thickness (mm)
0.5
0.4
0.3
0.2
0.1
0.0
600
700
800
1100
Spinning speed (RPM)

Figure S33